





Combined electrokinetic manipulations of pathogenic bacterial samples in low-cost fabricated dielectrophoretic devices

Cite as: AIP Advances 9, 115303 (2019); <https://doi.org/10.1063/1.5049148>

Submitted: 19 July 2018 . Accepted: 21 October 2019 . Published Online: 13 November 2019

Alejandro Martínez-Brenes, Karina Torres-Castro, Richard Marín-Benavides, Katherine Acuña-Umaña, Christopher Espinoza-Araya , Raquel Ramírez-Carranza, Gabriela González-Espinoza, Norman Rojas-Campos, Caterina Guzmán-Verri , Giovanni Sáenz-Arce , and Leonardo Lesser-Rojas 

COLLECTIONS

Paper published as part of the special topic on [Chemical Physics](#), [Energy, Fluids and Plasmas](#), [Materials Science](#) and [Mathematical Physics](#)



View Online



Export Citation



CrossMark

ARTICLES YOU MAY BE INTERESTED IN

[High-throughput continuous dielectrophoretic separation of neural stem cells](#)
Biomicrofluidics **13**, 064111 (2019); <https://doi.org/10.1063/1.5128797>

[Fifty years of dielectrophoretic cell separation technology](#)
Biomicrofluidics **10**, 032801 (2016); <https://doi.org/10.1063/1.4954841>

[Low frequency cyclical potentials for fine tuning insulator-based dielectrophoretic separations](#)
Biomicrofluidics **13**, 044114 (2019); <https://doi.org/10.1063/1.5115153>

AIP Advances Nanoscience Collection

READ NOW!

Combined electrokinetic manipulations of pathogenic bacterial samples in low-cost fabricated dielectrophoretic devices

Cite as: AIP Advances 9, 115303 (2019); doi: 10.1063/1.5049148

Submitted: 19 July 2018 • Accepted: 21 October 2019 •

Published Online: 13 November 2019



Alejandro Martínez-Brenes,^{1,2,3} Karina Torres-Castro,^{4,a)} Richard Marín-Benavides,^{5,6} Katherine Acuña-Umaña,^{2,3} Christopher Espinoza-Araya,⁷ Raquel Ramírez-Carranza,^{2,3} Gabriela González-Espinoza,⁸ Norman Rojas-Campos,⁸ Caterina Guzmán-Verri,⁹ Giovanni Sáenz-Arce,^{7,b)} and Leonardo Lesser-Rojas^{2,3,b)}

AFFILIATIONS

¹Maestría en Ingeniería en Dispositivos Médicos, Escuela de Ciencia e Ingeniería de los Materiales, Instituto Tecnológico de Costa Rica, 159-7050 Cartago, Costa Rica

²Laboratorio de Nano Bio Sistemas, Centro de Investigación en Ciencias Atómicas y Moleculares, Universidad de Costa Rica, 11501-2060 San José, Costa Rica

³Escuela de Física, Universidad de Costa Rica, 11501-2060 San José, Costa Rica

⁴Maestría en Electrónica con Énfasis en MEMS, Escuela de Ingeniería Electrónica, Instituto Tecnológico de Costa Rica, 159-7050 Cartago, Costa Rica

⁵Nanoscience and Technology Program, Taiwan International Graduate Program, Academia Sinica, 11529 Taipei, Taiwan

⁶Department of Physics, National Taiwan University, 10617 Taipei, Taiwan

⁷Laboratorio de Materiales Industriales, Departamento de Física, Universidad Nacional, 86-3000 Heredia, Costa Rica

⁸Centro de Investigación en Enfermedades Tropicales, Escuela de Microbiología, Universidad de Costa Rica, 11501-2060 San José, Costa Rica

⁹Programa de Investigación en Enfermedades Tropicales, Escuela de Medicina Veterinaria, Universidad Nacional, 304-3000 Heredia, Costa Rica

^{a)}Current address: Department of Electrical and Computer Engineering, University of Virginia, Charlottesville, VA 22904, USA.

^{b)}Authors to whom correspondence should be addressed: leonardo.lesser@ucr.ac.cr. Fax: (+506) 2253-7017. Postal address: Apartado Postal 11501-2060, San Pedro de Montes de Oca, San José, Costa Rica and gsaenz@una.cr. Fax: (+506) 2277-3344.

Postal address: Apartado Postal 86-3000, Heredia, Costa Rica.

ABSTRACT

A low-cost fabrication method of microfluidic devices with micrometer-sized constrictions used for electrodeless dielectrophoresis (eDEP) is demonstrated here. A structure on a commercial printed circuit board (PCB) template of one-sided copper clad fiberglass-epoxy laminate was used as a molding master for polydimethylsiloxane (PDMS) soft lithography. This was achieved by printing a constriction-based microchannel pattern on glossy paper with a micrometer-scaled resolution laser printer and transferring it to the laminate's Cu face, rendering a microstructure of $\sim 17 \mu\text{m}$ height and various widths across tips. The Cu master's pattern was transferred to PDMS, and smooth constrictions were observed under the microscope. Following air plasma encapsulation, PDMS chips were loaded with an inactivated bacterial sample of fluorescently stained *Brucella abortus* vaccine strain S-19 and connected to an amplified voltage source to examine the sample's response to electric field variations. After an AC/DC electric field was applied to the bacterial solution in the microfluidic device, the combined effect of electrokinetic + hydrodynamic mechanisms that interact near the dielectric microconstrictions and exert forces to the sample was observed and later confirmed by COMSOL simulations. Our fabrication method is an alternative to be used when there is no access to advanced micro-fabrication facilities and opens ways for target selection and preconcentration of intracellular pathogens as well as sample preparation for metagenomics.

© 2019 Author(s). All article content, except where otherwise noted, is licensed under a Creative Commons Attribution (CC BY) license (<http://creativecommons.org/licenses/by/4.0/>). <https://doi.org/10.1063/1.5049148>

I. INTRODUCTION

Members of the *Brucella* genus are facultative extracellular and intracellular α -proteobacteria responsible for causing brucellosis in a variety of mammals. This chronic disease can cause abortion and infertility in livestock with economic losses mainly in middle and low-income countries.¹ Humans are infected through direct contact with infected animals or through contaminated food products derived from infected animals. Brucellosis is considered by the World Health Organization (WHO) as a “forgotten neglected zoonosis,” estimating that for every reported human case, there are 25–50 unreported cases.² The ability to survive inside immune cells is a keystone for *Brucella* to cause disease, evading the innate immune response and causing unspecific symptoms which are easily confused with other infectious diseases.³ As with many infectious diseases, the available tools for diagnosis of brucellosis are limited, particularly in developing countries, leaving health care personnel without clear and opportune answers for effective treatment. It is in these settings where the chance for the outbreak of these pathogens increases.⁴

WHO has established basic criteria for an ideal diagnostic method of pathogens such as *Brucella abortus* in developing countries. Methods or devices to detect these pathogens must be economically accessible, user friendly, sensitive, specific, rapid, and not dependent on complex technology or nonportable energy.⁵ The miniaturization of diagnostic technology, thanks to micro- and nanotechnologies and the use of LOC (lab-on-chip) technologies,^{6,7} is a way to achieve the WHO criteria because it can handle complex chemical and biological management such as trapping, sorting, separation and patterning, purification characterization, and analysis.^{8–10} LOC microfluidic devices are also very attractive due to their capability of detecting microorganisms *in situ*. Previous work has demonstrated that low concentrations of the target bacteria are detectable through the use of electrokinetic preconcentration techniques such as dielectrophoresis (DEP).¹¹

DEP is the movement of particles in a nonuniform electric field due to the interaction of the particle's induced dipole and the spatial gradient of the electric field.^{12,13} When a dielectric particle is under the influence of an electric field, the particle becomes electrically polarized as a result of a partial charge separation, which leads to an induced dipole moment at the particle's surface. The induced dipole moment is either aligned with or directed against an applied field, resulting in positive or negative DEP, where the particle is attracted to or repelled from a region of high electric field strength, respectively.¹⁴ DEP trapping and levitation, electrorotation, and traveling-wave particle transport are examples of important applications of dielectrophoresis in biotechnology.¹⁵

DEP can manipulate biological particles such as bacteria, viruses, spores, yeast, and other types of eukaryotic cells in LOCs because of their favorable scaling for the reduced size of the system.¹² It has also been used to manipulate proteins,^{16–18} nucleic acids,¹⁹ and other types of biomolecules.¹² Pathogens such as *Escherichia coli*, *Clostridium difficile*, and *Cryptosporidium parvum* experience DEP and can be manipulated with a specific range of frequencies in an electrodeless DEP (eDEP) device, allowing characterizations and label-free separations of heterogeneous samples.^{20,21} Therefore, after lysis and filtering, DEP is the most suited technique to selectively preconcentrate *Brucella abortus* species and other

intracellular pathogens, which normally exist in very low concentrations in a blood sample from the infected host, thus making it easier to perform subsequent metagenomic studies.²²

However, when applying strong AC electric fields within an eDEP system, DEP is not always the only significant electrokinetic (EK) force and other nonlinear electrohydrodynamic (EHD) effects may give rise to fluid flows in the microfluidic channel which exert additional forces to the particles. The most relevant effects are induced charge electroosmosis (ICEO) and electrothermal flow (ET). ICEO is dependent on the induced charges on the surface of polydimethylsiloxane (PDMS)—a polarizable dielectric material with low but finite dielectric properties (conductivity and permittivity), exposed to an external electric field. ET emerges from the gradients in the intrinsic dielectric properties of the fluid due to Joule heating effects. Microvortex flow patterns near dielectric microconstrictions due to the combination of these long-range effects along with the short-range DEP have been reported to assist the trapping or deflection of particles in eDEP devices.^{23,24} These regions of recirculation, though, have mainly been avoided due to potential detrimental effects on both the medium and the bioparticles.²⁵

Nevertheless, some groups have reported eDEP devices using the combined effect of electrokinetic and hydrodynamic (HD) mechanisms harnessing vorticity to preconcentrate bioparticles. For instance, ET effects can enhance particle trapping and deflection by means of perturbing electrophoretic (EP) and electroosmotic flow (EOF) fields, creating vortices near the microchannel constriction.²⁶ Similarly, eDEP biomolecular trapping experiments can be assisted by ET flow vortices, enabled by long-range fluid sampling and localized stirring.²⁷ An example of the use of the enhancement of eDEP device efficiency is for the separation of a tumor cell by means of leveraging the vortex generation as a product of mixed hydrodynamic (HD) and EK phenomena.²⁸ In addition, eDEP with a DC field was employed to separate red blood cells (RBC) from plasma by combining nDEP, EOF, and HD force taking advantage of the channel geometry with stagnation zones.²⁹ However, the combined use of eDEP and vorticities arising from opposing direction flow profiles (hydrostatic pressure driven flow—HPDF and EOF) has not been reported before to aid the enrichment of bioparticles near the constriction tips.

Microfabrication technologies needed for DEP microfluidic LOCs require expensive equipment and facilities such as photolithography and metallic vapor deposition that are beyond the budget of the majority of institutions in developing nations.^{30–32} The introduction of polydimethylsiloxane (PDMS) has enabled fast and inexpensive fabrication of microfluidic LOC devices by “soft lithography” under normal benchtop conditions.^{33,34} In addition to being robust, flexible, biocompatible, and of low electrical and thermal conductivity, PDMS is also ideal since it can seal to a variety of materials. The major problem lies in the fabrication of SU-8 master molds for PDMS patterning, an expensive traditional photolithographic process. Hence, the development of low-cost molding master's fabrication techniques is imperative to do research in such scenarios.

A simpler alternative for fabricating microfluidic molds relies on the shrinkage properties of biaxially oriented polystyrene thermoplastic sheets; however, only rounded channel patterns can be achieved and limited reproducibility has been reported.³⁵ Direct-printing or toner transfer masking (TTM) has been used to

produce low-cost and disposable plastic-based microfluidic channel devices for on-chip applications without the need for clean-room facilities.^{36–38} The use of rapid marker and direct laser printing masking to replace photolithography, a similar fabrication method of microfluidic devices formed from replica molding of printed circuit board (PCB) copper-clad substrates, has been demonstrated. However, these patterns were either drawn or printed directly.^{39–41} Nevertheless, none of the abovementioned methods focuses on microfabricating devices for constriction-based eDEP manipulations. An earlier work introduced low cost technologies used to fabricate microfluidic DEP devices. However, the reported method used microelectrodes (Ti/Au or Cr/Au) patterned on a glass substrate and microchannels were fabricated using parylene, stereolithography-based resins, and SU-8.⁴²

In this work, we demonstrate a low-cost fabrication method of microfluidic devices with micrometer-sized constrictions for eDEP¹⁹ applications using a structure on a commercial FR-4 one sided copper clad PCB template, as a molding master for PDMS soft lithography. PDMS chips were later fabricated with a standard soft lithography procedure using the Cu master. The microchannel pattern was clearly transferred to PDMS, and smooth constrictions were observed under the microscope. Chips were later encapsulated with a cleaned cover glass, under air plasma activation conditions. To demonstrate functionality, PDMS chips were loaded with Texas Red Succinimidyl Ester (TRSE) stained inactive samples of *Brucella abortus* S-19 in an aqueous solution and imaged using an inverted fluorescence microscope. After an electric AC + DC field was applied to the bacterial solution in the microfluidic device, the combined effect of phenomena of DEP, EOF, and HPDF was observed near the constrictions, providing a proof of principle of an operational device suitable for particle enrichment.

II. MATERIALS AND METHODS

A. PDMS microfluidic device fabrication

The preparation of a Cu molding master is the experimental basis to create PDMS microchannels; its fabrication process is summarized in Fig. 1.

The pattern's design was made in a CAD software using two variables to control its shape, which allowed establishment of different initial conditions for the printing of the constrictions. Later, these patterns were printed on a glossy paper of 200 g/m² using a HP Color Laser Jet printer, model CP3525n [Fig. 1(a)]. For the construction of the mold, a commercial FR-4 PCB template of one sided ½ oz. copper clad fiberglass-epoxy laminate of 1.8 cm × 1.8 cm was used. The template was cleaned with acetone, isopropanol (IPA), and diH₂O in an ultrasonic bath for 5 min. After cleaning, the Cu template was positioned to the glossy paper's printed side by means of wetting the copper's surface with a 1 μl droplet of 99.5% IPA to facilitate the adhesion to the glossy paper [Fig. 1(b)]. The PCB + glossy paper with the ink pattern assembly was dried for 20 min on a hot plate at 165 °C by placing an iron on top of the assembly and allowing the system to reach thermal stability before manually pressing it [Fig. 1(c)]. After removing from the heat and pressure source and cooling down, the assembly was submerged in a container with diH₂O at room temperature for 20 s [Fig. 1(d)] and afterward, the glossy paper was peeled softly from the PCB template, leaving only the ink of the printed H-shape on the Cu's surface [Fig. 1(e)]. The surface of the copper plate was then rubbed with care to remove any remnant pieces of paper, rinsed again, and allowed to dry. Then, the PCB template was submerged in PCB etchant solution (GC Electronics, Rockford IL) under constant stirring for 15 min, and the H-shape design transferred to the copper surface served as a wet

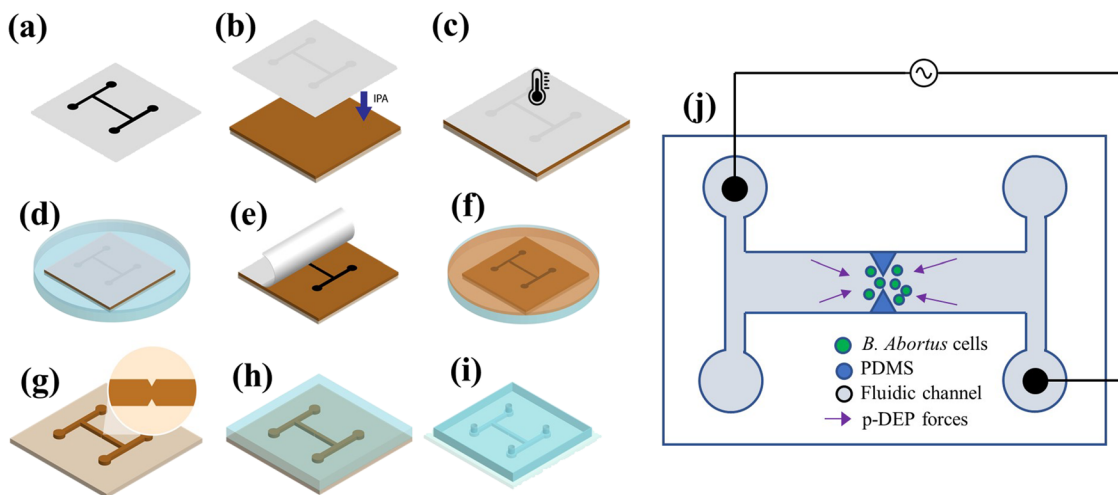


FIG. 1. Fabrication process of PDMS microfluidic device with microconstrictions: (a) H-shaped ink pattern was laser printed on a glossy paper with micrometer-scaled resolution. (b) The pattern was transferred to a laminate's copper sheet by contacting the glossy paper with 1 μl droplet of an organic solvent between surfaces and (c) heating the assembly on both sides and pressing it. (d) The assembly was submerged in DI water. (e) The glossy paper was removed leaving only the microchannel's ink masking pattern on the Cu's substrate. (f) Wet etching: PCB template is immersed in etching solution for 15 min under stirring. (g) Wet etching result: Ink-masked Cu remains, rendering a resulting H-structure that can serve as a master mold. A constriction is formed in the middle. (h) The Cu mold is used for PDMS soft lithography, (i) inlet through-hole punching and encapsulation, and (j) schematics of the device: 4 holes are used as inlet reservoirs for introducing sample and electrodes and to more effectively minimize static and dynamic pressure effects in the y-coordinate of the constriction channel. The region in the central channel is where particle enrichment and electrokinetic manipulation of the *B. abortus* cells are expected to occur.

etching mask, removing the copper in the exposed areas and leaving only the protected patterns [Figs. 1(f) and 1(g)]. Experiments were carried out previous to this last step to determine the etching rate of the etching solution at different dilution ratios (refer to the [supplementary material](#), Sec. I), and the resulting steplike feature was measured using a profilometer (Bruker's DektakXT[®] Stylus Profiler).

Inside a laminar flow hood, the Cu molds were cleaned following a standard semiconductor cleaning protocol using acetone, isopropyl alcohol, and diH₂O sonicator baths and later blown with a N₂ gun to remove the ink mask as well as any residues and particles that could be present on the mold's surface.

Measurements of the resulting pattern widths of microconstrictions in all stages of the process were performed using optical microscopy and a Zeta-20 Optical Profiler (Zeta Instruments, San Jose, CA).

Micromolding was performed using PDMS (Sylgard[®] 184, Dow Corning, Midland, MI) in 10:1 proportion with the curing agent. The mixture was placed in a vacuum desiccator for 20 min to remove bubbles. Magic Tape (3M, Maplewood, MN) was used to create a molding cage around the master, and the PDMS mixture was poured slowly to cover ~0.5 cm in height. A vacuum desiccator was used for 10 min for removing the bubbles formed in the pouring process. Afterward, PDMS was cured in a preheated muffle furnace at 80 °C for 2 h and then peeled off from the copper mold [Fig. 1(h)]. Through holes serving as fluidic reservoirs and the inlets for the injection of microorganisms were punched on the circular regions of the resulting PDMS structure.

Coverslips were cleaned to remove organic residues and films following the RCA-1 or "standard clean-1," based on sequential oxidative desorption and complexing with H₂O₂-NH₄OH-H₂O (1:1:5), then heated to 70 °C and soaked in the solution for 15 min, and later transferred to a container with overflowing DI water to rinse and remove the solution.

Room air plasma produced in a commercial plasma cleaner (Harrick Plasma, PDC-32G) was used to promote surface activation and subsequent bonding between RCA-1 cleaned coverslips and the PDMS chips,³⁶ thus allowing the encapsulation of the microfluidic channels [Fig. 1(i)].

An illustrative scheme is shown in Fig. 1(j). Since the idea is to enrich particles of the *B. abortus* cells in the central microchannel, we chose an H-shaped microfluidic channel architecture with 4 loading reservoirs, which were used as inlet channels for introducing sample and AgPt electrodes, and with a central microchannel containing dielectric microconstrictions where EK manipulations take place.⁴³

B. Inactivated *Brucella* cells solution

B. abortus vaccine strain S-19 was grown in a broth media for 24 h. Bacteria were killed after exposure to a 1.5% bleach solution, centrifuged, and resuspended in water. Survival tests were performed to assure that bacteria were killed.

Bleach-inactivated cultures of *B. abortus* S19 were centrifuged at 2500 g for 5 min and washed twice in phosphate-buffered saline (PBS) at room temperature. Cell pellets were resuspended with Texas Red Succinimidyl Ester (TRSE, EX 595 nm, EM 605 nm, Invitrogen[™]) in PBS at a concentration of 1 μg/ml and incubated

for 30 min in the dark. The bacteria were then washed twice in PBS and observed using a fluorescence microscope. A highly concentrated S-19 in solution was obtained, and its concentration value of 3.2×10^9 CFU/ml was determined using a spectrophotometer.

A 1:10 diluted solution from the original concentrated solution was used in the experiments. The conductivity of the solution was measured using a conductivity meter (Horiba, LAQUAtwin EC-22). Diluted solutions of inactivated *B. abortus* vaccine strain S-19 previously stained with Texas Red were injected to the microfluidic chip.

C. Experimental setup

Fluorescent inactivated bacterial solution was loaded in our device and observed at 40× magnification in an inverted fluorescence microscope (Leica DM18) with a mercury metal halide bulb (Leica EL6000) as the light source and a Y3 filter cube (Leica, Exc: 545/23 nm; mirror: 565 nm; Em: 605/70 nm). A commercial wave-form generator (Keysight 3350013 Series) was used to produce an AC signal which was amplified through a high voltage linear amplifier (FLC Electronics AB A400) and used to apply an AC/DC E-field across the chip's fluidic reservoirs using electrodes to induce the particle's electrokinetic response. An oscilloscope (BK Precision) was used to observe the variation of the signal supplied by the source. The results were recorded using a scientific sCMOS camera (Andor Technologies, Zyla 4.2 PLUS).

D. Computational modeling with finite element analysis

COMSOL Multiphysics[®] version 5.4.0.295 (Palo Alto, CA) was used to evaluate the feasibility of our low-cost fabricated eDEP microfluidic device with microconstrictions for the preconcentration of inactivated *Brucella* cells by the combined effect of electrokinetic and hydrodynamic phenomena. The device was simulated by modeling a 2D-model geometry which encloses a conductive buffer where *Brucella* particles are immersed. The model was built using the following physics modules: creeping flow (microfluidic module) to model the fluid flow in the microfluidic device; electric currents (AC/DC module) to model the electric field distributions; heat transfer (heat transfer in fluids module) to study the Joule heating effect in the fluid; and particle tracing for fluid flow (particle tracing module) to solve for the trajectories of particles experiencing drag and dielectrophoretic forces (refer to the [supplementary material](#), Sec. II, for the underlying equations solved for the simulation, model description, parameters, and boundary conditions).

III. RESULTS AND DISCUSSION

Measurements were performed using optical microscopy and an optical profiler to characterize the structures produced at each step of the fabrication process. First, the structure printed with ink on the glossy paper was observed, as shown in Fig. 2(a), finding that the ink's thickness was (1.9 ± 0.2) μm and constrictions could be printed down to ~160 μm (mean width). However, as shown in Fig. 2(b), constrictions became wider and less pronounced during the ink transfer to the PCB surface, possibly due to heat expansion and wetting effects. After chemical etching, the thickness of

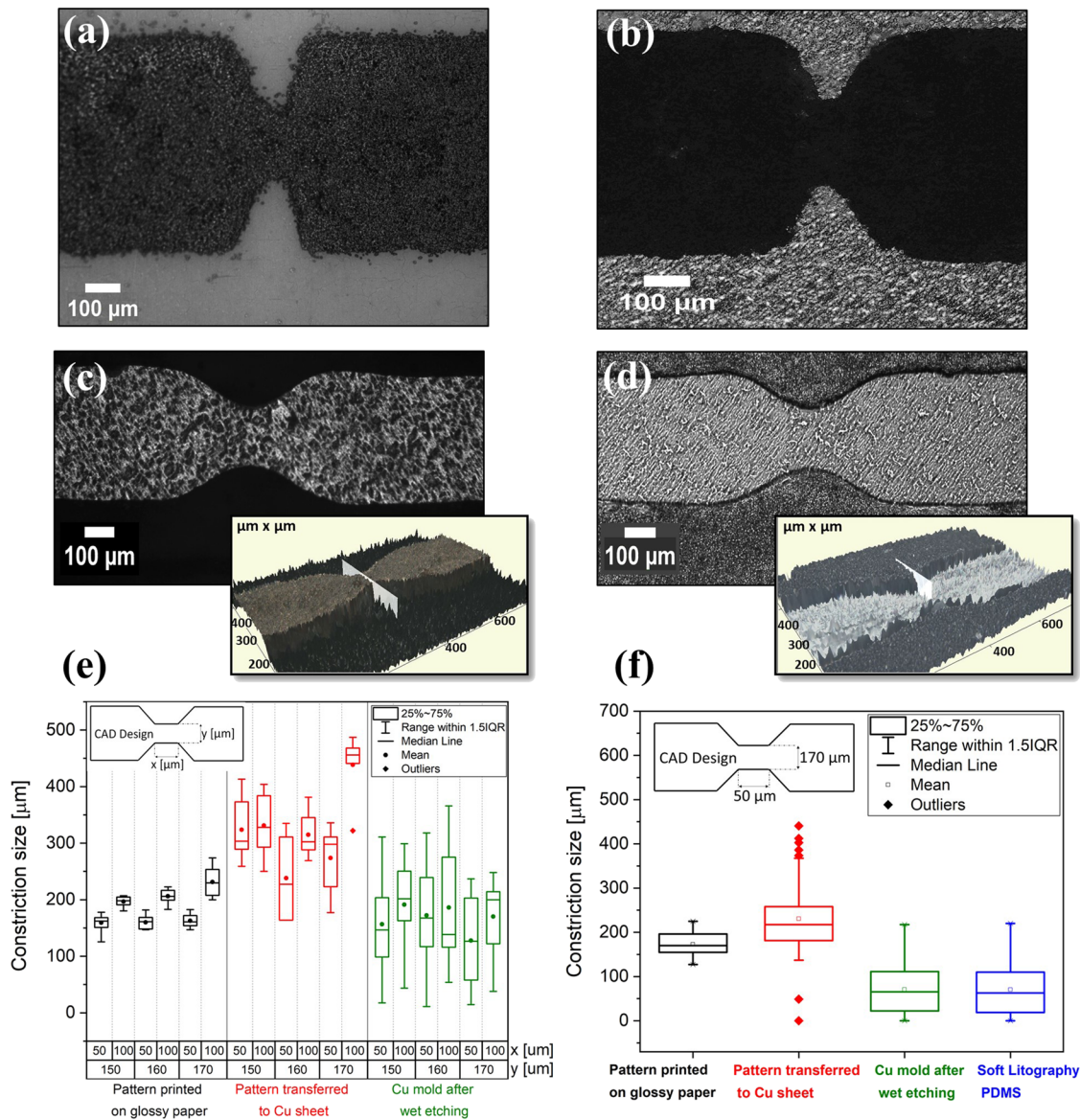


FIG. 2. (a) Optical micrography of a $175.3 \mu\text{m}$ wide constriction pattern laser-printed on glossy paper with a $(1.9 \pm 0.2) \mu\text{m}$ thick top layer of ink, (b) optical micrography of a $235 \mu\text{m}$ wide constriction pattern, after the same ink pattern in (a) was heat transferred to the PCB's Cu sheet. (c) Optical micrography top view of a $139.3 \mu\text{m}$ wide constriction pattern, after the same pattern in (b) was wet etched, defining a PCB based molding master. The inset shows the optical profilometry 3D view with a $(16.3 \pm 0.8) \mu\text{m}$ thick layer of Cu and (d) optical micrography top view of a $155.4 \mu\text{m}$ wide constriction pattern in the microchannel, after the same pattern in (c) was replicated using PDMS micromolding. The inset shows the corresponding optical profilometry of a $(20.3 \pm 0.5) \mu\text{m}$ deep feature. (e) Statistical box plot comparison of measured results within the different fabrication steps ($N_{\text{samples}} = 12$ for each geometry) and different design parameters height (x) and width (y). (f) Further fabrication experiments with a higher sample size ($N_{\text{samples}} = 78$), for the design condition $x = 50 \mu\text{m}$ and $y = 170 \mu\text{m}$ [outlier points were included in the calculation of the whiskers following the 1.5 interquartile range (1.5IQR) method].

copper was $(16.3 \pm 0.8) \mu\text{m}$ with a surface roughness, R_a , of $0.9 \mu\text{m}$ [Fig. 2(c)], as expected from the information offered by the manufacturer (clad copper thickness: $17 \mu\text{m}$).

Values of the constriction width were measured at each step of the fabrication process, as shown in Fig. 2(e). Printing a CAD design with a sharp microconstriction was not suitable for achieving reproducible results due to the spatial resolution of the

printer. To overcome this limitation, we optimized the design and found that defining a channel described by two main design parameters height (x) and width (y) [Fig. 2(e) inset] results in an ink printed pattern with a mean micrometer constriction width of $(186 \pm 22) \mu\text{m}$ in the glossy paper. The range of the channel parameters for which proper microconstrictions were obtained is $50\text{--}100 \mu\text{m}$ in (x) and $150\text{--}170 \mu\text{m}$ in (y).

Although the constriction width increases to mean values of $(320 \pm 66) \mu\text{m}$ due to thermal expansion when transferring the ink pattern to the copper substrate, during the chemical etching process, the constriction width decreases to features of $(167 \pm 133) \mu\text{m}$ which are smaller than the former ink pattern, due to isotropic etching effects.

Deviations in the fabrication process shown in Fig. 2(e) might arise starting from the nature of inkjet printing process and its resolution, continuing with the ink expansion during the heat transfer process as well as differences in the copper etching arising from the position of the measured pattern in the wafer (such as thermal gradients and different removal speeds created by the orbital shaking of the etchant solution at the center and the outside radius locations of the wafer), thus locally influencing the conditions such as the ink expansion and copper etch-rate and finally the size of the patterns in each step.

The results of etch-rate tests established that a 25% etchant concentration was suitable to achieve an etch rate of Cu at $1.3 \mu\text{m}/\text{min}$, thus slowing down the etching-rate from pure etchant solution by 6.5-fold and controlling undercuts to achieve smaller constrictions. In some cases, Cu master molds with $\sim 20 \mu\text{m}$ microconstriction sizes were achieved (refer to the [supplementary material](#), Sec. III), these values being comparable to what can be achieved with the standard photolithography method.²⁰

A strategy to improve the statistics started from reducing the number of features in the wafer so that they remain localized in a central region where thermal and etchant stirring conditions are almost constant. The results of further fabrication experiments with a higher sample size ($N = 78$) that took into consideration the aforementioned strategy are shown in Fig. 2(f). These were performed for the design condition $x = 50 \mu\text{m}$, $y = 170 \mu\text{m}$, which was the one with the smallest mean constriction value for the pattern transferred to Cu sheet in Fig. 2(e), showing an increase in the number of data falling in the range between the first and the third quartiles (25%–75%) and within the 1.5 interquartile range (1.5IQR) (refer to the [supplementary material](#), Sec. III).

Transferring the ink pattern to the laminate's Cu sheet was the process with the highest deviations, possibly due to the nonuniform application of pressure on top of the PCB + glossy paper with the ink pattern assembly toward the hotplate using an iron which in turn leads to a nonuniform heat distribution, thus affecting the repeatability and scatter of the data, as shown in Fig. 2(f). A future strategy to correct this part of the process relies on the use of a heat press transfer machine similar to those used in sublimation printing, which might help for the application of uniform heat and pressure conditions to the assembly and reduce the variation in this process.

After PDMS micromolding with the resulting copper masters, microchannels of $(20.3 \pm 0.5) \mu\text{m}$ depth with slightly pronounced microconstrictions were successfully replicated in the middle of H's central microchannel. An example of the resulting microstructure is shown in Fig. 2(d). Later on, a plasma encapsulation process took place. This last step does not seem to be a low-cost procedure as it requires a high price equipment that can put into question the overall cost of the device. Alternately, a plasma corona wand could be used to activate surfaces⁴⁴ and reduce the fabrication cost further.

As a proof of principle of the device's operation and capability of handling the bioparticle of interest, experiments were attempted with the inactivated *Brucella* cells. After injection of solution at

the chip's inlet reservoir, a capillary flow was observed within the channels.

Experiments were performed with both concentrated and diluted solutions. In a first line of experiments, the concentrated solution was used, having a conductivity of $\sigma = 25 \mu\text{S}/\text{cm}$.

Without the application of any electrical field, there is still a unidirectional movement of the fluid and the S-19 bacterial particles toward one end of the microfluidic channel, mainly due to hydrostatic pressure driven flow (HPDF) coming from column height differences between the reservoirs. To reduce HPDF, droplets with exact volumes on two fluidic reservoirs located on opposite sides of the device were placed after the initial filling process and allowing the system to balance itself for few minutes until it reached equilibrium. Despite the effort, the HPDF could not be completely ruled out. In order to compensate for this situation, a DC voltage was applied, creating an electroosmotic flow (EOF) in the reverse direction of the HPDF and forcing the fluid and the S-19 particles to temporarily stop when the value of the potential was +9 V. The reversibility of this effect was confirmed several times switching the DC voltage on and off. The increase in the DC voltage above the +9 V value eventually overcomes the equilibrium and generates a flow reversal that carries the bacterial particles toward the opposite direction from the one that they were originally moving due to HPDF. Later, this counteracting DC voltage was applied as an offset of the AC signal that was expected to generate DEP. Parameters for DEP separation were found fixing the AC voltage amplitude value and performing a variable frequency sweep, doing one experiment at a time. AC voltage amplitude was changed between 10 and 400Vpp, while AC frequency was swept from 200 kHz up to 1 MHz for each voltage amplitude value, until the values of 400 Vpp and 1 MHz were reached, and thus, the effect of preconcentrating the bacterial particles near the constrictions upon the application of the AC-biased electric field was observed. An increase in fluorescence was registered, as shown in Fig. 3(b) (Multimedia view).

Figure 3(c) shows the fluorescence intensity vs time, plotted from a $25 \mu\text{m}^2$ area [~ 100 pixels, shown in a circle in the inset of Fig. 3(d)] on a region of high intensity of fluorescence near the constriction, to which the background was subtracted. It could be observed how under the application of the combined E-fields, as time passes, more fluorescent-stained bacterial particles are accumulated near the dielectric constriction, thus rapidly increasing in less than 1 s the fluorescence intensity level from the initial background of ~ 20 a.u. until reaching saturation between fourfold to fivefold of that value. This effect is reversible, and one could also observe that after switching the AC biased voltage off, the fluorescence intensity starts decreasing until it returns near the initial background level in ~ 1.5 s.

The point of evaluation of the fluorescence intensity shown in Fig. 3(c) was a convenient region of interest since no fluorescent particles were nonspecifically bound to the PDMS surface at that spot, and it was in alignment with a band of highest fluorescence intensity where the preconcentrating effect was taking place, therefore allowing the fluorescence quantification. However, there were also other regions near the middle of the microfluidic channel which are away from the tip of the dielectric material that forms the constriction and which remain dark, and where the fluorescent particles swirl and pass-by in a rapid manner that suggests that under the AC + DC field scenario, pressure-driven flow has not been completely suppressed.

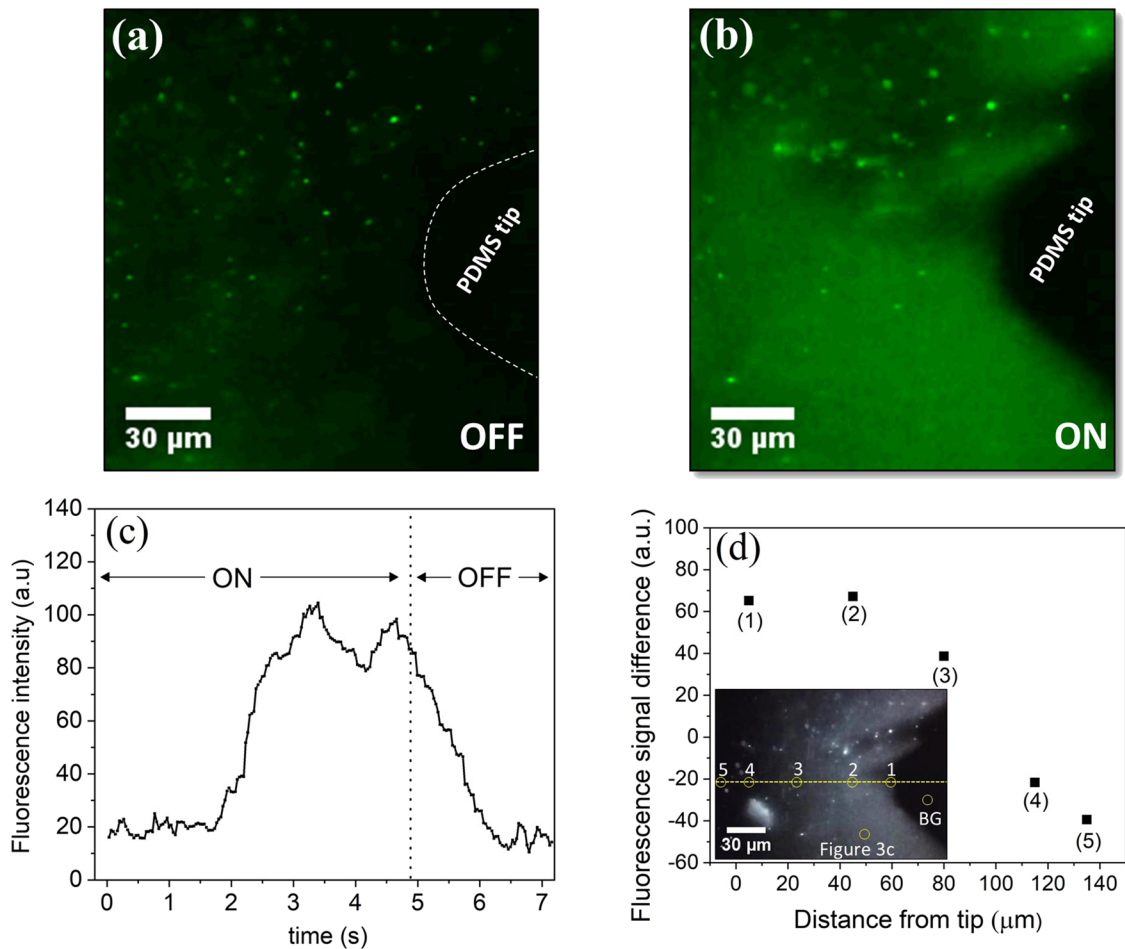


FIG. 3. Positive preconcentration of inactivated particles of *B. abortus* S-19 in a concentrated solution ($\sigma = 25 \mu\text{S}/\text{cm}$), around a $360 \mu\text{m}$ wide PDMS microconstriction. (a) Without applying an AC field, (b) applying an AC field at $1 \text{ MHz} | 400\text{V}_{\text{pp}} | +9 \text{ V DC}$ bias, (c) fluorescence intensity vs time (background corrected) with an ON-OFF cycle of the AC-biased field as in (b), averaged from a circular region of interest of $25 \mu\text{m}^2$ (~ 100 pixels) shown in an inset in (d), and (d) fluorescence signal difference vs distance from tip, measured and averaged at different evaluation circular regions along the central line collinear to the midpoint of the constriction's axis (inset). Fluorescence intensity difference was measured between the upper and lower fluorescence intensity asymptotic values during the "ON" part of the AC-biased field cycle (see the [supplementary material](#), Sec. IV, for the individual line graphs and the calculation of asymptotes using a sigmoidal fitting). Multimedia view: (b): <https://doi.org/10.1063/1.5049148.1>

It is important to mention that the fluorescent particles, which contribute to a strong background fluorescence in certain spots that are unchanged in position or intensity in [Figs. 3\(a\)](#) and [3\(b\)](#), may correspond to larger aggregates or clusters of inactivated bacterial cells, nonspecifically adhered to surface areas where the roughness is the biggest due to the PDMS reverse copy of the cooper's surface [such as the one seen in [Fig. 2\(c\)](#)]. Due to the high bacterial cell concentration in the solution, *Brucella* cell's small size, cells' high velocity, the use of a middle objective magnification ($40\times$), and the low-number of frames per second (fps) used in the camera operation, it was not possible to resolve the individual nonaggregated bacterial cells in [Fig. 3\(b\)](#) (Multimedia view).

In order to understand such fluorescence intensity distribution, later we quantified the fluorescence accumulation in different points ($5 \mu\text{m}$, $45 \mu\text{m}$, $80 \mu\text{m}$, $115 \mu\text{m}$, and $135 \mu\text{m}$) distanced along the

central line collinear to the midpoint of the constriction's axis, as seen in the inset of [Fig. 3\(d\)](#) inset, and these data are shown in [Fig. 3\(d\)](#). Each point refers to the difference between the upper and lower asymptotes calculated from a sigmoidal fitting for each of the fluorescence graphs shown in [Fig. S8](#) that provide a numerical value close to the mean value of the fluorescence intensity fluctuation in the levels before preconcentration and after preconcentration (refer to the [supplementary material](#), Sec. IV).

Results show that the further the evaluation spot is from the constriction tip, the lower the fluorescence intensity increase during the application of the AC+DC fields, and finally, near the center of the microfluidic channel, there is a fluorescence intensity decrease (negative fluorescence signal difference), due to the lower particle concentration. The phenomenon was observed several times, occurring similarly in all cases, and it was possibly due to a combination

of DEP, EOF, and HPDF driven forces interacting near the dielectric constriction.^{39,40} The mechanism of rapid fluorescence intensity decreases after turning the AC biased field off may be due to a restored dominant HPDF coming from column height differences between the reservoirs. HPDF is faster than diffusional mechanisms, which was in-line with the rapid particle movement we observed.

In order to understand the full extent of the complex phenomena observed, Multiphysics COMSOL parametric calculations were performed to evaluate the distribution, variation, and influence of the DEP, EOF, and HPDF driven forces in our device, as well as the influence of Joule heating induced flows. Velocity fluid flow profiles, E-field distribution, particle tracing, and temperature

distribution simulations were performed in our microchannel device (for details on the geometric model and used parameters, see the [supplementary material](#), Sec. II). The result of FEM solutions in the region around the dielectric constriction, with a similar geometry and working parameters as the device used in the experiments; is shown in Fig. 4.

The result of FEM solutions for ∇E_{rms}^2 around the dielectric constriction, with a similar geometry and E-field conditions as the device used in the experiments, is shown in Fig. 4(a). The result shows that the E-field gradient (DEP term) is the highest near the apex of the dielectric tip that forms the constriction and decays rapidly over a distance along the central line collinear to the

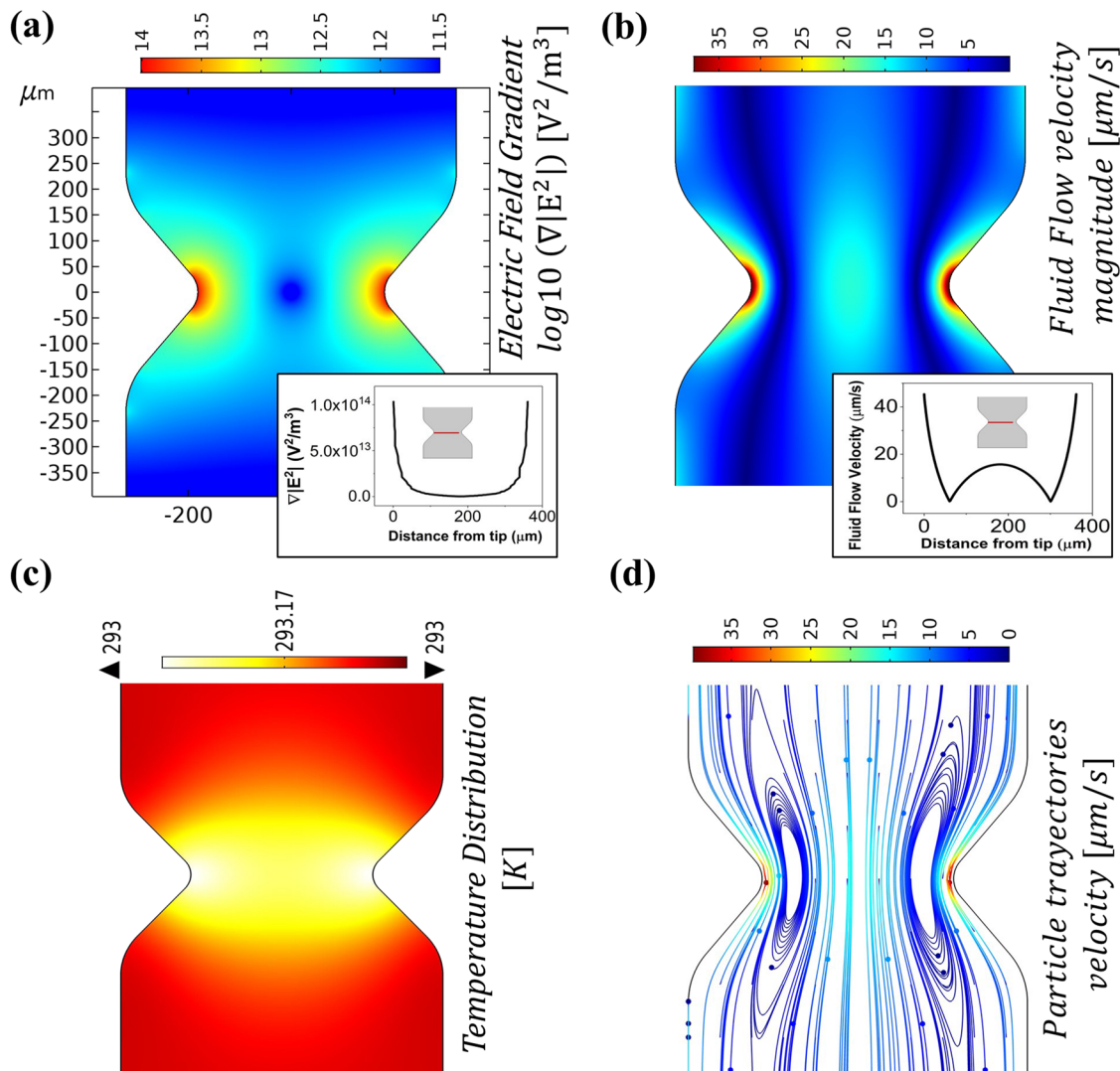


FIG. 4. COMSOL simulations: (a) Distribution of the gradient square of the electric field in base-10 log scale [$\log_{10}(\nabla E_{rms}^2)$] in the chip with a microconstriction width of $360 \mu\text{m}$ and an applied voltage of $400V_{pp}$ and (inset) distance from tip (r_{ex}) along the channel width direction at the constriction center ($y = 0$) line-probed from (a), (b) creeping flow velocity magnitude profile and (inset) creeping flow velocity magnitudes along the channel width direction at the constriction center ($y = 0$) line-probed from (b), (c) temperature distribution, and (d) particle trajectories due to the particle's response to the tracing force $\mathbf{F}_t = (\mathbf{F}_{drag} + \mathbf{F}_{DEP})$ in the device. Multimedia view: (d): <https://doi.org/10.1063/1.5049148.2>

constriction's axis, as seen in the inset of Fig. 4(a). For DEP spatial manipulation of *B. abortus* S-19 bacterial particles, in order to trap and draw them toward the constrictions, electric forces must exceed diffusion and friction. The minimum force needed to overcome these effects can be defined as an observable deterministic threshold force F_{th} , and this corresponds to a threshold $\nabla E_{rms}^2 \sim 5.69 \times 10^{13} \text{ V}^2/\text{m}^3$ for a bacterial particle of a $0.5 \mu\text{m}$ radius (refer to the supplementary material, Sec. V, for more details). This number is smaller than the $1.11 \times 10^{14} \text{ V}^2/\text{m}^3$ maximum value obtained from the simulation at the dielectric tip's wall. The distance from tip (r_{ex}) along the probe line in the inset of Fig. 4(a), at which the value ∇E_{rms}^2 that was obtained from the COMSOL simulation equals the threshold's is $5.08 \mu\text{m}$. The constriction width across dielectric tips ($360 \mu\text{m}$) is large and thus favorable only for short-range DEP manipulation. However, the scenario changes for larger bacterial particle radii, $1.0 \mu\text{m}$ and $1.5 \mu\text{m}$, where the threshold ∇E_{rms}^2 values become $1.01 \times 10^{13} \text{ V}^2/\text{m}^3$ and $3.65 \times 10^{12} \text{ V}^2/\text{m}^3$, thus extending r_{ex} to $47.76 \mu\text{m}$ and $84.68 \mu\text{m}$, respectively. Bacterial particle interactions as well as cell-cell associations could also be occurring, which are normally not considered in computational models and experimental discussions of DEP phenomena,⁴³ and that could increase the range of DEP's influence over larger distances, as we observed in our experiments.

Moreover (and as shown by our simulations), DEP is not the only existing mechanism that could aid the collection of bacterial particles in our device. The DC offset's field distribution near the dielectric walls causes effects involving EO mobility which in combination with the hydrostatic pressure head parabolic profile (which is due to the pressure-difference balancing) causes the formation of high speed flow regions in the reverse direction one from each other which are located near the wall surface and the center of the microfluidic channel, as well as a slow speed or "meadow" region located between those, as seen in Fig. 4(b). An inlet flow (velocity inlet condition of $0.5 \mu\text{m}/\text{s}$) was used which could take into account the HPDF influence in the simulation. The superimposed phenomenon is evident in the inset of Fig. 4(b), which shows the fluid flow velocity profile measured using a probe line along the channel width (x) direction at the constriction center in Fig. 4(b), where the high velocity near the surface of the microchannel's wall has a value of $\sim 45 \mu\text{m}/\text{s}$ due to EOF, which decreases away from the tip of the constriction until reaching a minimum value close to $0 \mu\text{m}/\text{s}$ at $x = 60 \mu\text{m}$, and a central high velocity band that extends beyond this point until reaching a maximum velocity of $16 \mu\text{m}/\text{s}$ near the center of the microchannel ($x = 180 \mu\text{m}$) due to HPDF. Interestingly, the location of the minimum fluid velocity value or "meadow" at $x = 60 \mu\text{m}$ corresponds to the region between the two points with highest fluorescence intensity in Fig. 3(d), where particle accumulation seems to take place. The temperature distribution result [Fig. 4(c)] shows that there is only a small temperature rise of 0.02 K in the vicinity of the constrictions, as a result of a low fluid conductivity value, thus ruling out the possible generation of electrothermal flows due to Joule heating.

Therefore, DEP is not the only mechanism that traps particle near the vicinity of the dielectric tip but possibly also the abovementioned combined long-range effect involving HP and DC bias-induced EO flows, which form microvortex flow patterns near the dielectric microconstrictions. This looks to be overcoming the short-range ∇E_{rms}^2 effective threshold limitations for small particle

radii, collecting also in a band that extends $\sim 90 \mu\text{m}$ from the tip of the constriction, which is an unachievable effective distance by pure DEP means as derived from our E-field calculations, thus making the preconcentration possible without the need of small constrictions.

Simulations include COMSOL's particle tracing for the fluid flow module using $0.5 \mu\text{m}$ diameter particles with double shell properties (see the supplementary material, Sec. II, for details), which simulated dielectric particles that mimic *Brucella*'s gram-negative cell wall to obtain the particle trajectories and their dielectrophoretic force F_{DEP} + particle drag force F_{drag} response, proof that the assumption is correct, as particles near the "meadow" or small velocity region get trapped in a vortexlike manner due to the combination of the effects, and those near the central region of the microfluidic channel that are far away from the DEP + low flow velocity region do not get trapped in the vortex and pass rapidly driven by the HPDF, as seen in Fig. 4(d) (Multimedia view).

As suggested by the Classius-Mossoti factor (C.M.) for microbial gram-negative double shell cells such as *B. abortus*, at intermediate low-buffer conductivities, the effect of frequency is crucial to observe the experimental preconcentration of the composite bioparticles. For such microbial cells, the less conductive cell wall and the capacitive cell membrane around the conducting cytoplasmic region cause a polarization dispersion over a large frequency range. Only at these high frequencies, the electric field leaks through the insulating shell to cause cytoplasmic polarization, which triggers a strong pDEP response. There is also an effect of microbial shape on the polarization dispersion: the higher particle eccentricity causes higher pDEP levels at lower cytoplasmic polarization peak level values compared to their spherical counterparts, as well as lower first crossover frequency values around the 1 MHz range.⁴⁵ At low frequencies, where nDEP is dominant (C.M. < 0), bacterial particles are possibly pushed away from the vortex and into low velocity flow "meadows" toward the central high speed fluid velocity region formed during the application of the AC + DC fields, therefore getting swept away in a rapid manner that avoids their observation, possibly in a fashion as seen on the experimental data points 4 and 5 from Fig. 3(d) and the COMSOL simulation. Moreover, low-frequency regimes below 200 kHz were avoided to elude AC-electroosmotic effects which would have compete with F_{DEP} .⁴⁶ On the other hand, the AC-voltage amplitude effect mainly determines the magnitude of F_{DEP} but not the translational direction of the particles. Regularly, in eDEP devices, the electrodes are far from each other in the microfluidic channel (in our case 1 cm apart), and thus, high AC-voltage amplitudes are required in order to consider F_{DEP} .²⁵

In this first experiment, the highly concentrated S-19 in solution ($3.2 \times 10^9 \text{ CFU}/\text{ml}$) made it difficult to confirm the proposed hypothesis since the observation of a single particle's response in the collective motion was not possible. For these aforementioned reasons, a second set of experiments were performed. A 1:10 diluted solution from the original concentrated stock solution was used, which was diluted in a solvent of less conductivity (in purified H_2O type II final electrical conductivity of sample: $\sigma = 5\text{--}6 \mu\text{S}/\text{cm}$). This strategy was used as it is favorable to reduce the particle's concentration and the medium conductivity value as reducing it further can result in a change from nDEP to pDEP for a long range of low frequencies below 1 MHz ⁴⁷ and as seen by our simulations (see the supplementary material, Sec. II, for more details), making the DEP force push particles toward strong field regions.²³ The constriction

width across dielectric tips and the applied AC field were reduced by half of the original 360 μm and 400 V_{pp} figures, to 180 μm and to 200 V_{pp} respectively, in order to scale down the effective ∇E_{rms}^2 value. A counteracting DC voltage was applied as an offset of the AC signal that generates DEP. AC-voltage amplitude was set, and the frequency was swept setting one voltage amplitude value at a time for each frequency sweeping experiment, starting from 10 V_{pp} and 200 kHz, respectively, until reaching the values of 200 V_{pp} and 320 kHz where electrokinetic effects were obtained. The results of the application of these conditions near the constriction region can be observed in Fig. 5 (Multimedia view).

It is observed from Fig. 5(a) (Multimedia view) that the enclosed particle moves in circles in a vortexlike fashion near the apex of the constriction after getting initially attracted, due again to the possible combination of short-range DEP + HPDF and DC bias-induced EOF long-range effects.

Except from those following the microvortexes, most of the other bacterial particles far from the constriction tip and near the center of the microfluidic channel are strongly influenced by the HPDF and continue their movement. Some other particles (or larger aggregates) that remain static even before and after the application of E-fields might have attached to the PDMS surface due to nonspecific adhesion,⁴⁸ but the rest is moving because of the abovementioned effects. Rugosity in the surface of PDMS as well as the line roughness of the Cu mold near the constrictions may also be playing a role in the observed effects as molecular dynamic simulations have demonstrated that the ion distributions of the double electrical layer could be strongly affected by surface roughness, making it less effective in concave regions compared to flat surfaces, decreasing the EOF speed as well as the zeta potential.^{49,50} The nonspecific adhesion of some particles near the constrictions could be also related to this fact.

A particle tracking analysis [Fig. 5(b) (Multimedia view)] was performed to quantitatively describe the observed vortexlike trajectory shown by the bacterial particle under study (Multimedia view). The position of the centroid of the fluorescent spots representing the particle of interest was tracked at each frame using an in-house MATLAB code. Image processing procedures such as averaging, normalization, and binarization were performed previous to the particle tracking to isolate the particle of interest and assess the tracking clearly. The pixel positions were transformed to micrometer displacements, and the curve was fitted by a sinusoidal function. The velocity of the particle was obtained by deriving the fitted function with respect to time. The inset of Fig. 5(b) (Multimedia view) shows the time-dependent displacement and velocity of the particle. The particle trajectory suggests to be following a general harmonic movement that describes a sinusoidal oscillation $y = y_0 + A * \sin(\pi \frac{x-x_c}{\omega})$ (see the supplementary material, Sec. VI, for more details), with a period $T \sim 1.4$ s. The particle periodically reaches a maximum velocity of 22.5 $\mu\text{m/s}$ in a position distanced approximately at $x = 5\text{--}8$ μm away from the shadow of the constriction's apex along the (x) channel width direction at the constriction center ($y = 0$). The observed combined effect is reversible, and the moment the E-field is switched-off, initial conditions where the bacterial particles are just flowing toward one direction in the microchannel due to HPDF are observed again.

In this case, the scenario of combination of short-range DEP+ long-range HPDF and DC bias-induced EOF is demonstrated again by our simulations. The DC E-field near the dielectric constrictions

causes EO mobility which is superimposed to the HPDF flowing in the reverse direction. This phenomenon is evident in Fig. 5(c), which shows that the creeping flow velocity profile measured using a probe line along the channel width (x) direction at the constriction center displays the same two regions of velocity, the first one near the surface of the constriction where the fluid velocity reaches the speed value of 22.5 $\mu\text{m/s}$ at $x = 2.5$ μm and then decreases away from the tip of the constriction until reaching a minimum value close to 0.4 $\mu\text{m/s}$ at $\sim x = 50$ μm , and a central velocity band that extends beyond this point until reaching a maximum near the center of the microchannel. The positions are in good agreement with the experimental measurement of the location where the bacterial particle's speed reaches its maximum value as uncertainties in the measurement of the particle's position away from the constriction's edge may arise due to border rugosity and the isotropic profile of the microchannel's wall. Figure 5(d) (Multimedia view) shows the result of COMSOL's simulations that include particle tracing for fluid flow module, proving that the vortexlike movement of the particles is due to the combination of the described effects (Multimedia view). In a similar fashion as in the 360 μm constriction, the applied AC voltage does not generate a significant temperature increase, thus ruling out ET effects due to Joule heating (see the supplementary material, Sec. II, for results).

A parametric study evaluating the effects of the applied AC voltage, the particle radius, and the constriction width on the pre-concentration capability of the device was performed using COMSOL, using the global evaluation feature during postprocessing in order to count the total number of particles in a defined domain (which was a region of interest near the constrictions). COMSOL results suggested that as long as the conditions of the parabolic profile in one direction due to HPDF and the plug profile in the other direction produced by the EOF are maintained, the generation of vortexes will still occur, which in combination with DEP will effectively trap and preconcentrate the number of particles in the device. Particles of larger radius (1.0–1.5 μm) when in combination with larger applied AC voltage experience significant contributions from the DEP term and appear to accumulate near to the constriction in a more evident fashion (see the supplementary material, Sec. V, for more information).

Experiments to improve the ink printing resolution and controlled wet-etching transfer of the features to achieve the fabrication of more pronounced microconstrictions are currently undergoing. A possible way to improve the current constriction size-limitation will rely on printing with high-resolution printers (20 000 dpi or higher), in order to reduce the constriction size of the ink feature. The use of a high resolution printer, in combination with application of uniform heat and pressure to the assembly during the ink transfer process to the Cu's laminate (using a heat press transfer machine), and fine control over the etching rates of the chemical wet etchant, might accurately reproduce dielectric constrictions of sizes below 100 μm which could be an alternative to conventional fabrication of DEP devices and result in the application of these in conventional eDEP separation strategies.²⁵ The use of these strategies with either external fluid flow and/or applied DC bias could help enrich particles. Constriction size reduction increases the E-field gradient focusing effect, making it easier to observe/control in detail the desired phenomena and to study its effect on individual particles in order to fully characterize the pathogen's response to frequency variations.

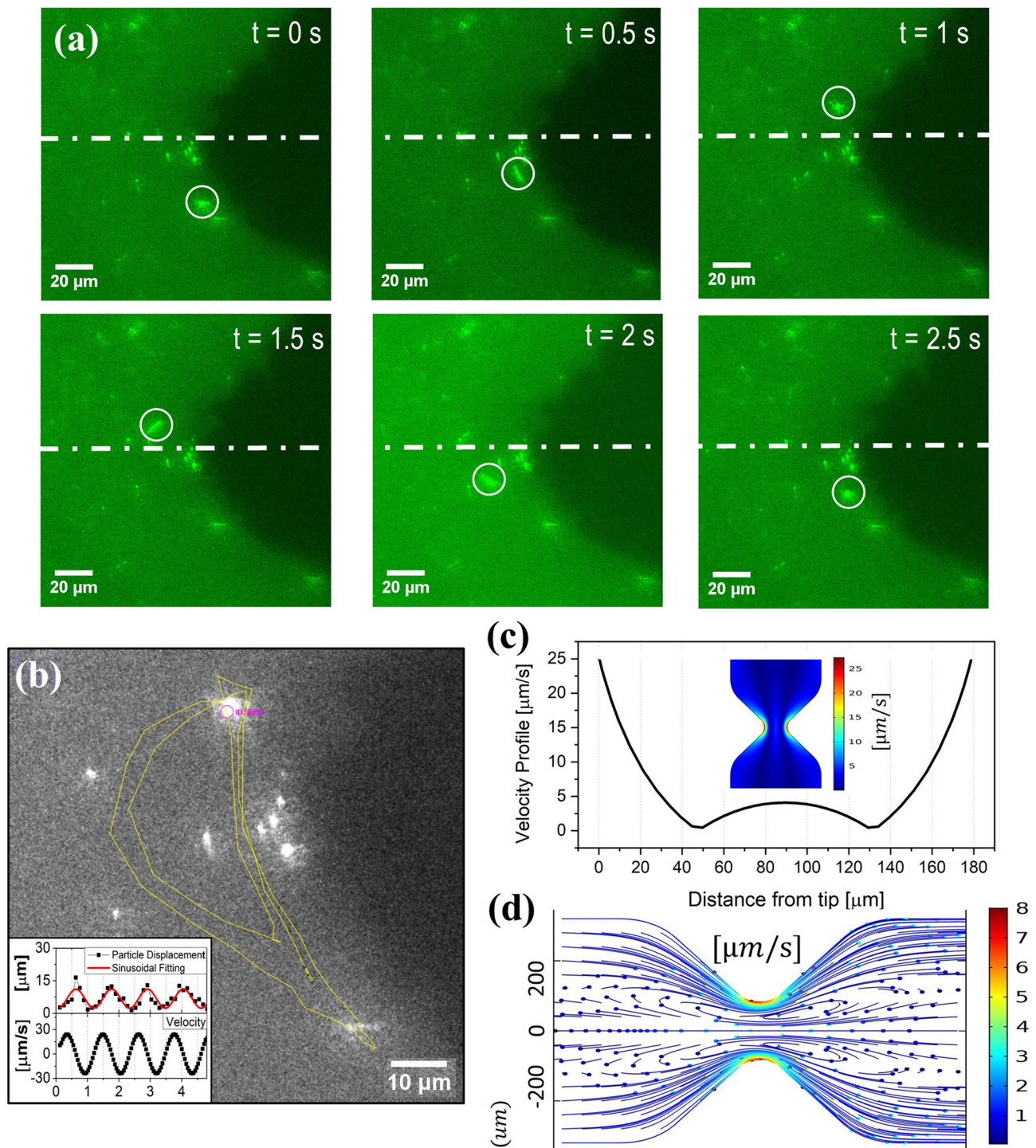


FIG. 5. (a) Time-lapsed electrokinetic response of inactivated particles of *B. abortus* S-19 in a dissolved solution ($\sigma = 6 \mu\text{S/cm}$) around the PDMS microconstriction ($180 \mu\text{m}$) when applying an amplified AC field at 320 kHz | 200Vpp | -3 V DC bias (images were pseudocolored for illustration purposes). (b) Vortexlike trajectory (yellow line) of the particle near the constriction, experiencing combined short and long-range electrokinetic phenomena and (inset) displacement and velocity of the first 4 cycles of the trajectory of the particle vs time fitted with a sinusoidal function. (c) Creeping flow velocity magnitudes along the channel width direction at the constriction center ($y = 0$) line-probed from (inset) creeping flow velocity magnitude profile. (d) Particle trajectories due to the particle's response to the tracing force $F_t = (F_{\text{drag}} + F_{\text{DEP}})$ in the device. Multimedia views: [(a), (b), and (d)]: <https://doi.org/10.1063/1.5049148.3>; <https://doi.org/10.1063/1.5049148.4>; <https://doi.org/10.1063/1.5049148.5>

Nonspecific adhesion of some bacterial particles/aggregates on the PDMS surface could be avoided by using surface blocking agents⁴⁸ and will be examined in future experiments in order to reduce this effect.

Future work also plans to focus on a systematic study of the observed combined electrokinetic phenomena with model polystyrene fluorescent particles of known physical properties, in order to experimentally understand the in-depth kinetics of the current particle enrichment scenario. Nevertheless, the performed proof-of-concept experiment demonstrated that the microchip's fabrication and encapsulation of constrictionlike structures are possible with our proposed low-cost method and that electrokinetic pre-concentration of pathogenic samples of interest under the current experimental setup is feasible.

IV. CONCLUSIONS

To summarize, a micromolding method for the fabrication of PDMS constrictionlike microstructures using a low-cost copper master was demonstrated. A microchannel pattern was clearly transferred to the PDMS, and smooth constrictions were observed under the microscope. Differences in the measured constriction widths in each step of the fabrication process were characterized using a statistical analysis which shows how the two main design parameters in the CAD file influence the result of the final constriction width. However, these values were not always reproducible and the results span over a large Gaussian distribution, for which further tests with controlled conditions and a larger sample size were performed and those helped to significantly enhance the statistics.

PDMS chips were loaded with an inactivated *B. abortus* S-19 bacterial sample. Different conditions of AC field frequency and amplitudes were applied, and various electrokinetic effects were observed on the device which are attributed to the combined effect of short-range dielectrophoretic (DEP) + long range-electroosmotic (EO), and hydrostatic pressure (HP) driven flows, which allowed the vortexlike movement of collective and individual inactivated *B. abortus* particles observed around the tip of the dielectric constrictions in aqueous solutions, as validated by our experiments and COMSOL simulations. Nevertheless, it was confirmed that these phenomena are reversible for the majority of the particles and occur only after the AC+DC fields are applied.

Our fabrication method could be used in nations that lack advanced microfabrication facilities and may open up simple ways for target selection and manipulation of intracellular infectious pathogens and its later implementation on a method of obtaining appropriate enriched samples for metagenomic studies.

SUPPLEMENTARY MATERIAL

Refer to the [supplementary material](#) for more information about complementary details of the fabrication process, the underlying equations, model description, parameters and boundary conditions used for the COMSOL simulation, the calculation of the distance from tip (r_{ex}), as well as the parametric study evaluating the effect of the applied AC voltage, the particle radius, and the constriction width on the preconcentration capability of the device. A growth/sigmoidal fitting to provide values of fluorescence intensity differences in [Fig. 3\(d\)](#) (Multimedia view) and sinusoidal fitting

results to the displacement of the particle of interest in [Fig. 5\(b\)](#) (Multimedia view) are also detailed.

ACKNOWLEDGMENTS

This study was funded by the Fondos del Sistema del Consejo Nacional de Rectores (FEES-CONARE) Costa Rica, project name: “Cerrando la brecha entre el diagnóstico convencional de enfermedades infecciosas y el diagnóstico de nueva generación.” We thank Professor Nathan Swami and John H. Moore II, Department of Electrical and Computer Engineering, University of Virginia (UVA), for helpful discussions and English language editing of the manuscript, respectively. L.L.-R. thanks Dr. K. K. Sriram from Chalmers University of Technology, Gothenburg, Sweden, and Dr. Thierry Leïchlé from LAAS-CNRS, Toulouse, France, for their critical reading of the original manuscript. We acknowledge the Centro de Investigación en Electroquímica y Energía Química (CELEQ), Universidad de Costa Rica, for access to their cleanroom facilities and to Professors Mavis Montero and Leslie Pineda for their support to K.T.-C.'s thesis project. G.S.-A. thanks Dr. Ricardo Starbird and Alex Fernando Alvarado Hidalgo (Instituto Tecnológico de Costa Rica) and Dr. Esteban Avendaño-Soto (CICIMA-UCR) for their help with profiler measurements, and C.G.-V. thanks Daphne Garita from the Tropical Diseases Research Programme (PIET), Veterinary School, Universidad Nacional, for technical support.

REFERENCES

- 1 E. Moreno and I. Moriyón, in *The Prokaryotes*, edited by M. Dworkin, S. Falkow, E. Rosenberg, K.-H. Schleifer, and E. Stackebrandt (Springer New York, New York, 2007), pp. 315–456.
- 2 WHO Department of Control of Neglected Tropical Diseases, *The Control of Neglected Zoonotic Diseases: From Advocacy to Action* (WHO Press, Geneva, 2015).
- 3 E. Barquero-Calvo, E. Chaves-Olarte, D. S. Weiss, C. Guzmán-Verri, C. Chacón-Díaz, A. Rucavado, I. Moriyón, and E. Moreno, *PLoS One* **2**, e631 (2007).
- 4 GAO General Accounting Office, Global Health, *Challenges in Improving Infectious Disease Surveillance Systems* (United States General Accounting Office, Washington, DC, 2001).
- 5 M. Urdea, L. A. Penny, S. S. Olmsted, M. Y. Giovanni, P. Kaspar, A. Shepherd, P. Wilson, C. A. Dahl, S. Buchsbaum, G. Moeller, and D. C. Hay Burgess, *Nature* **444**(S1), 73 (2006).
- 6 D. Figeys and D. Pinto, *Anal. Chem.* **72**, 330A (2000).
- 7 Y. C. Lim, A. Z. Kouzani, and W. Duan, *Microsyst. Technol.* **16**, 1995 (2010).
- 8 D. G. Grier, *Nature* **424**, 810 (2003).
- 9 S. Haeberle and R. Zengerle, *Lab Chip* **7**, 1094 (2007).
- 10 D. Mark, S. Haeberle, G. Roth, F. von Stetten, and R. Zengerle, *Chem. Soc. Rev.* **39**, 1153 (2010).
- 11 T. F. Didar and M. Tabrizian, *Lab Chip* **10**, 3043 (2010).
- 12 B. Cetin and D. Li, *Electrophoresis* **32**, 2410 (2011).
- 13 H. A. Pohl, *Dielectrophoresis: The Behavior of Neutral Matter in Nonuniform Electric Fields* (Cambridge University Press, Cambridge, 1978).
- 14 R. Pethig, *Biomicrofluidics* **4**, 022811 (2010).
- 15 T. B. Jones, *IEEE Eng. Med. Biol. Mag.* **22**, 33 (2003).
- 16 K.-T. Liao and C.-F. Chou, *J. Am. Chem. Soc.* **134**, 8742 (2012).
- 17 K.-T. Liao, M. Tsegaye, V. Chaurey, C.-F. Chou, and N. S. Swami, *Electrophoresis* **33**, 1958 (2012).
- 18 L. Lesser-Rojas, P. Ebbinghaus, G. Vasan, M.-L. Chu, A. Erbe, and C.-F. Chou, *Nano Lett.* **14**, 2242 (2014).
- 19 C.-F. Chou, J. O. Tegenfeldt, O. Bakajin, S. S. Chan, E. C. Cox, N. Darnton, T. Duke, and R. H. Austin, *Biophys. J.* **83**, 2170 (2002).

- ²⁰Y.-H. Su, C. A. Warren, R. L. Guerrant, and N. S. Swami, *Anal. Chem.* **86**, 10855 (2014).
- ²¹Y.-H. Su, M. Tsegaye, W. Varhue, K.-T. Liao, L. S. Abebe, J. A. Smith, R. L. Guerrant, and N. S. Swami, *Analyst* **139**, 66 (2014).
- ²²E. Chaves-Olarte, C. Guzmán-Verri, E. Paramithiotis, and E. Moreno, in *Brucella: Molecular Microbiology and Genomics*, edited by I. López-Goñi and D. O'Callaghan (Caister Academic Press, Norfolk, 2012), pp. 103–131.
- ²³Q. Wang, N. N. Dingari, and C. R. Buie, *Electrophoresis* **38**, 2576 (2017).
- ²⁴X. Xuan, B. Xu, D. Sinton, and D. Li, *Lab Chip* **4**, 230 (2004).
- ²⁵B. H. Lapizco-Encinas, *Electrophoresis* **40**, 358 (2019).
- ²⁶B. G. Hawkins and B. J. Kirby, *Electrophoresis* **31**, 3622 (2010).
- ²⁷V. Chaurey, C. Polanco, C.-F. Chou, and N. S. Swami, *Biomicrofluidics* **6**, 012806 (2012).
- ²⁸A. Aghilinejad, M. Aghaamoo, X. Chen, and J. Xu, *Electrophoresis* **39**, 869 (2018).
- ²⁹M. Mohammadi, H. Madadi, J. Casals-Terré, and J. Sellarès, *Anal. Bioanal. Chem.* **407**, 4733 (2015).
- ³⁰R. Pethig, *J. Electrochem. Soc.* **164**, B3049 (2017).
- ³¹M. Li, W. H. Li, J. Zhang, G. Alici, and W. Wen, *J. Phys. D: Appl. Phys.* **47**, 063001 (2014).
- ³²R. Martinez-Duarte, *Electrophoresis* **33**, 3110 (2012).
- ³³J. C. McDonald and G. M. Whitesides, *Acc. Chem. Res.* **35**, 491 (2002).
- ³⁴J. C. McDonald, D. C. Duffy, J. R. Anderson, D. T. Chiu, H. Wu, O. J. Schueller, and G. M. Whitesides, *Electrophoresis* **21**, 27 (2000).
- ³⁵A. Grimes, D. N. Breslauer, M. Long, J. Pegan, L. P. Lee, and M. Khine, *Lab Chip* **8**, 170 (2008).
- ³⁶W. K. T. Coltro, D. P. de Jesus, J. A. F. da Silva, C. L. do Lago, and E. Carrilho, *Electrophoresis* **31**, 2487 (2010).
- ³⁷E. de Oliveira Lobo, Jr., L. da Costa Duarte, L. E. de Paula Braga, Á. L. Gobbi, D. P. de Jesus, and W. K. T. Coltro, *Microsyst. Technol.* **21**, 1345 (2015).
- ³⁸C. J. Easley, R. K. P. Benninger, J. H. Shaver, W. Steven Head, and D. W. Piston, *Lab Chip* **9**, 1119 (2009).
- ³⁹M. Abdelgawad, M. W. L. Watson, E. W. K. Young, J. M. Mudrik, M. D. Ungrin, and A. R. Wheeler, *Lab Chip* **8**, 1379 (2008).
- ⁴⁰A. P. Sudarsan and V. M. Ugaz, *Anal. Chem.* **76**, 3229 (2004).
- ⁴¹M. Abdelgawad and A. R. Wheeler, *Microfluid. Nanofluid.* **4**, 349 (2008).
- ⁴²S. Rajaraman, S.-O. Choi, R. H. Shafer, J. D. Ross, J. Vukasinovic, Y. Choi, S. P. DeWeerth, A. Glezer, and M. G. Allen, *J. Micromech. Microeng.* **17**, 163 (2007).
- ⁴³J. O. Tegenfeldt, C. Prinz, H. Cao, R. L. Huang, R. H. Austin, S. Y. Chou, E. C. Cox, and J. C. Sturm, *Anal. Bioanal. Chem.* **378**, 1678 (2004).
- ⁴⁴A. Lalonde, A. Gencoglu, M. F. Romero-Creel, K. S. Koppula, and B. H. Lapizco-Encinas, *J. Chromatogr. A* **1344**, 99 (2014).
- ⁴⁵R. E. Fernandez, A. Rohani, V. Farmehini, and N. S. Swami, *Anal. Chim. Acta* **966**, 11 (2017).
- ⁴⁶Y. Ren, W. Liu, Y. Tao, M. Hui, and Q. Wu, *Micromachines* **9**, 102 (2018).
- ⁴⁷J. Cebricos, R. Hoptowit, and S. Jun, *LWT* **80**, 185 (2017).
- ⁴⁸H. Zhang and M. Chiao, *J. Med. Biol. Eng.* **35**, 143 (2015).
- ⁴⁹R. Qiao, *Microfluid. Nanofluid.* **3**, 33 (2007).
- ⁵⁰P. Lu, X. Liu, and C. Zhang, *Micromachines* **8**, 190 (2017).